

PROJECT FOR PRECISION MEASUREMENT OF THE PROTON CHARGE RADIUS IN AN ELECTRON-PROTON SCATTERING EXPERIMENT

PNPI participants in the collaboration ^{*)}:

**A.A. Vorobyev, A.A. Vasilyev, S.L. Belostotsky, B.V. Bochyn, A.A. Dzyuba, G.E. Gavrillov,
V.T. Grachev, K.A. Ivshin, A.G. Inglessi, P.V. Kravchenko, P.A. Kravtsov, E.M. Maev,
S.M. Mikirtychanz, P.V. Neustroev, G.E. Petrov, N.R. Sagidova, A.N. Solovyev, I.N. Solovyev,
E.M. Spiridenkov, V.A. Trofimov, M.E. Vznuzdaev**

^{*)} *Petersburg Nuclear Physics Institute, Russia;
Institute for Nuclear Physics, University of Mainz, Germany;
Joint Institute for Nuclear Research, Dubna, Russia;
GSI Helmholtzzentrum für Schwerionenforschung, Germany;
William and Mary College, USA;
Mount Allison University, Canada;
University of Regina, Canada;
Saint Mary's University, Canada*

1. Introduction

This project is motivated by the striking discrepancy (4%) between precise measurements of the proton charge *rms*-radius $R_p = \langle R_{pE}^2 \rangle^{1/2}$ in the muonic hydrogen (μH atoms) Lamb shift experiments performed at PSI by the CREMA Collaboration ($R_p = 0.84184(87)$ fm [1], $R_p = 0.84087(39)$ fm [2]) and the radius determined in the electron-proton (ep) elastic scattering experiments: $R_p = 0.879(5)_{\text{stat}}(6)_{\text{syst}}$ fm, A1 collaboration at Mainz [3], and $R_p = 0.875(10)$ fm, Thomas Jefferson National Accelerator Facility [4].

The “proton radius puzzle” is widely discussed in the scientific community. Various reasons for the observed discrepancy are under discussion, including possible existence of an exotic particle coupling differently to electrons and muons (physics beyond the Standard Model). It is generally agreed that new ep elastic scattering experiments are needed to resolve this puzzle.

In the ep elastic scattering experiments, the proton charge radius is extracted from the slope of the electric form factor at the momentum transfer squared $Q^2 \rightarrow 0$. The A1 Collaboration at MAMI obtained the most accurate data set on ep scattering consisting of more than 1400 points in the momentum transfer range of $0.004 \text{ GeV}^2 \leq Q^2 \leq 1 \text{ GeV}^2$, and the result of this measurement proved to be now in strong disagreement with the values determined in the muonic hydrogen Lamb shift experiments. A similar result was obtained in the ep scattering experiments performed at the Thomas Jefferson National Accelerator Facility.

However, these results are under discussion at present. The problem is that the available experimental data in the low Q^2 region are not sufficient for precision extraction of the proton radius. Therefore, extrapolation from higher Q^2 regions is used, and the result becomes dependent on the assumed Q^2 shape of the proton form factors. This was demonstrated in some recent analyses of the A1 experimental data [5].

Another problem might be related to application of the radiative corrections to the measured differential cross sections. In all previous ep scattering experiments, the differential cross sections were determined by measuring the angular distribution of the scattered electrons selected by momentum with magnetic spectrometers. In this case, the radiative corrections are quite large ($\sim 10\%$), depending on the selection procedure of the scattered electrons. The radiative corrections are Q^2 dependent and they may influence the extracted value of the proton radius. In principle, the level of the introduced radiative corrections could be controlled by the absolute measurements of the differential cross sections. However, no such measurements exist until today. In this context, new high-precision data on ep scattering in the low Q^2 region, including absolute measurements of the differential cross sections, are highly desired.

The first new generation ep scattering experiment aimed at precision measurement of the proton radius is the PRad experiment at Jlab [6]. In this experiment, the electron scattering on a hydrogen gas jet-like target will be studied in the Q^2 range from $2 \cdot 10^{-4} \text{ GeV}^2$ to $8 \cdot 10^{-2} \text{ GeV}^2$ at 1.1 GeV and 2.2 GeV beam energies.

The angle and the energy of the scattered electron are detected with a forward tracker and a forward calorimeter. The estimated radiative corrections will be at the level of 15%. The elastic ep scattering cross sections will be normalized to the simultaneously measured Møller scattering cross section. The PRad experiment started taking data in 2016. The goal is to reach a sub-percent precision in R_p .

The experiment described in this project will use an innovative method allowing for detection of recoil protons and scattered electrons at low Q^2 with high accuracy and resolution, thus leading to a completely new approach for extraction of the proton radius. The goal is to measure the ep differential cross sections in the Q^2 range from 0.001 GeV² to 0.04 GeV² with 0.1% relative and 0.2% absolute precision and to determine the proton radius with a sub-percent precision. An important advantage of the applied method is considerably lower radiative corrections inherent to the recoil proton method controlled, in addition, by the absolute measurement of the differential cross sections.

The experiment will be performed at the Mainz electron accelerator MAMI. This accelerator can provide an electron beam with practically ideal for this experiment parameters, as it was demonstrated in a special test run in September 2017. The Proposal was approved by the MAMI Program Advisory Committee, and a special Agreement aimed at realization of this experiment was signed between PNPI and INP Mainz.

2. Experimental overview

The ep elastic scattering differential cross section at high electron energies is given by the following expression:

$$\frac{d\sigma}{dt} = \frac{\pi\alpha^2}{t^2} \left\{ G_E^2 \left[\frac{(4M + t/\varepsilon_e)^2}{4M^2 - t} + \frac{t}{\varepsilon_e^2} \right] - \frac{t}{4M^2} G_M^2 \left[\frac{(4M + t/\varepsilon_e)^2}{4M^2 - t} - \frac{t}{\varepsilon_e^2} \right] \right\}, \quad (1)$$

where $\alpha = 1/137$, ε_e – the initial total electron energy, M – the proton mass, $t = -Q^2 = -2MT_R$, T_R – the recoil proton energy, G_E – the electric form factor, G_M – the magnetic form factor. At low Q^2 , the form factors G_E and G_M can be represented by the power series expansions:

$$G_{E,M}(Q^2)/G_{E,M}(0) = 1 - \langle R_p^2 \rangle Q^2 / 6 + \langle R_p^4 \rangle Q^4 / 120 - \langle R_p^6 \rangle Q^6 / 5040 + \dots \quad (2)$$

Here R_p stands for R_{pE} or R_{pM} – the proton charge and magnetic radii, respectively. The proton charge radius can be determined from the slope of the electric form factor G_E at $Q^2 \rightarrow 0$. An example of $d\sigma/dt$ in the small Q^2 region is shown in Fig. 1.

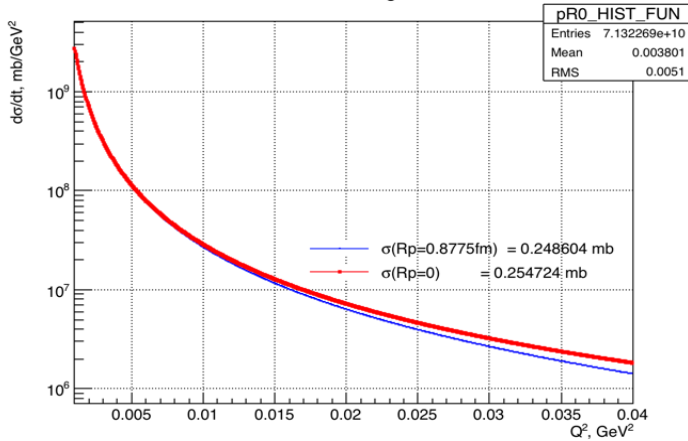


Fig. 1. Differential cross section for ep elastic scattering at $\varepsilon_e = 720$ MeV calculated for $R_p = 0$ and for $R_p = 0.8775$ fm following from a modified Dipole Form Factor

The differential cross sections will be measured for $\varepsilon_e = 720$ MeV in the Q^2 range from 0.001 GeV² to 0.04 GeV². The sensitivity of $d\sigma/dt$ to the proton radius in this Q^2 range is rather low, as it is demonstrated in Fig. 2. The cross sections corresponding to $R_p = 0.88$ fm and $R_p = 0.84$ fm differ only by 1.3% at $Q^2 = 0.02$ GeV². That means that at least 0.2% precision in measurements of $d\sigma/dt$ is needed to distinguish reliably between these two options. ***In this experiment, the differential cross sections will be measured with 0.1% relative and 0.2% absolute precision.***

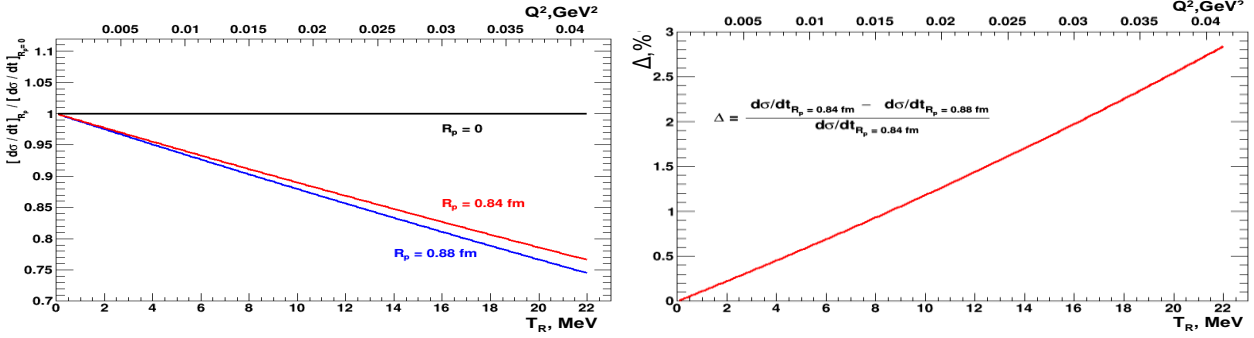


Fig. 2. Ratio of $d\sigma/dt$ calculated for two different values of R_p to that calculated for the point-like proton (left panel). Difference between the ep differential cross sections corresponding to $R_p = 0.84$ fm and $R_p = 0.88$ fm (right panel)

3. Experimental method

An active hydrogen target – a Time Projection Chamber (TPC) detecting recoil protons will be used in combination with a high precision Forward Tracker (FT) detecting the scattered electrons. The hydrogen TPC was first developed at PNPI, and it was used in several experiments [7–9] including experiments WA9 and NA8 at CERN for studies of small-angle πp and pp scattering at high energies. A new advanced version of the hydrogen TPC will be used in this experiment.

Figure 3 shows a schematic view of the proposed experimental set-up. It consists of a hydrogen TPC with a MWPC based Forward Tracker and a beam monitoring system. The TPC operates in the ionization mode (no gas amplification). It allows to measure the recoil proton energy T_R , the recoil proton angle θ_R , and the Z -coordinate of the vertex Z_V . The Cathode-Grid distance (drift space) is $400.00 \text{ mm} \pm 40 \text{ }\mu\text{m}$. The Anode-Grid distance is 10 mm. Grid: $100 \text{ }\mu\text{m}$ wires with 1 mm wire spacing. The anode is subdivided into a central pad (10 mm diameter) surrounded by 7 rings (40 mm width each) plus an outer ring (15 mm width). The anode outer diameter is 600 mm (Fig. 4). The TPC will operate at two gas pressures, 20 bar and 4 bar, with the maximal energy of the protons stopped in the TPC sensitive volume 10 MeV and 4 MeV, respectively. For higher proton energies, the TPC measures the energy deposited in the sensitive volume (for example, 5 MeV for 20 MeV protons at 20 bar H_2) and the angle. Also, there is a possibility to use the CH_4 gas filling. In this case the maximal energy of the protons stopped inside the TPC is 22 MeV (Fig. 4).

The forward tracker (FT) is designed for high absolute precision in measuring the X and Y coordinates of the electron track relative to the beam line. Also, it measures the arrival times of the scattered electrons. The FT acceptance is from 4 mrad to 460 mrad, which provides full coverage of the θ_e distribution corresponding to the selected Q^2 range at the electron beam energy 500 MeV – 720 MeV (Fig. 4). The FT consists of two pairs of Cathode Strip Chambers (CSC): X_1/Y_1 and X_2/Y_2 . Each chamber is a symmetric MWPC with a 3.0 mm gap between the cathode and the anode planes. The size of the chamber is $600 \times 600 \text{ mm}^2$. The readout is from both cathode planes. The anode wire plane contains $30 \text{ }\mu\text{m}$ wires spaced by 3 mm. Both cathode planes are made of $50 \text{ }\mu\text{m}$ wires wound with 0.5 mm step. The cathode wires are orthogonal to the anode wires in one cathode plane and inclined by 45 deg. in the other cathode plane. The wires in the inclined cathode plane are grouped into 10 mm strips. The key element of the CSC is the cathode plane with orthogonal cathode-to-anode wires. It determines the absolute measurements of the coordinate along the anode wire. In this plane, 2.5 mm strips are formed by joining together 5 wires. Using the centre-of-gravity method, the coordinate of each detected track is determined with $\sim 30 \text{ }\mu\text{m}$ resolution.

The CSC strip plane is fabricated in such a way that it provides the absolute linear scale with $\sim 0.02\%$ precision.

The FT and TPC are assembled in a common vessel in separated volumes. The TPC operates with ultra-clean hydrogen at up to 20 bar gas pressure, while the $\text{Ar} + 2\% \text{CH}_4$ gas mixture is used in the FT at the gas pressure equalized with that in the TPC. The gas purity and pressure will be maintained by special gas circulation/purification systems. The gas gain in the MWPCs varies from 10^3 to 10^4 for 20 bar and 4 bar pressure, respectively. There is a dead zone in the centres of the CSCs (20 mm in diameter) to reduce the sensitivity to the electron beam crossing the CSCs. This is done by electrolytically depositing an additional

gold layer on the anode wire in this spot. Note that some sensitivity still remains, and it will be used in the detector alignment procedure.

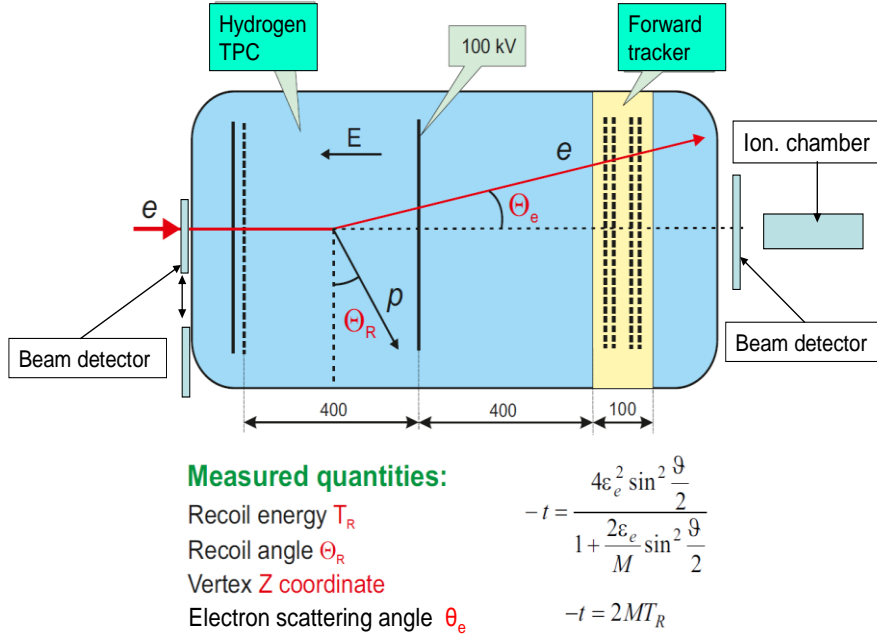
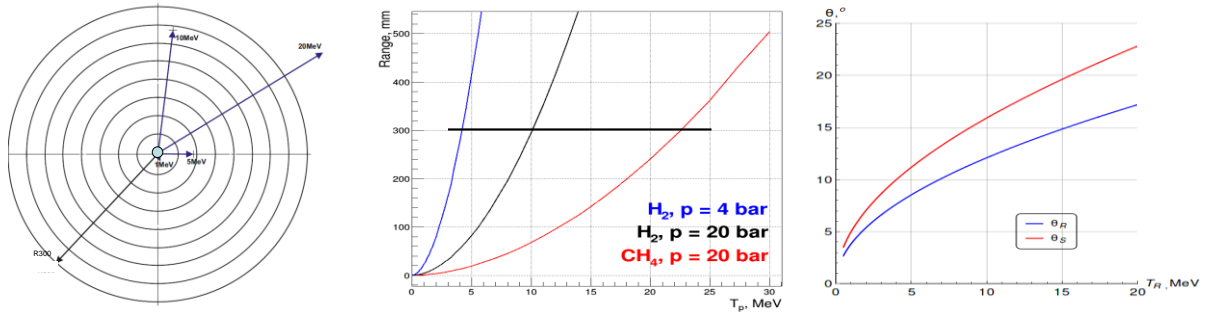


Fig. 3. Schematic view of the combined TPC & FT detectors



The beam detectors have several functions:

1. tracing the beam line and control for beam stability;
2. measuring the arrival times of the beam electrons;
3. absolute counting of the beam electrons for determination of the absolute cross section.

The first of these functions is provided by the Pixel detectors, which were successfully tested in the 2017 test run ($3 \times 3 \text{ mm}^2$ size, $80 \times 100 \text{ }\mu\text{m}^2$ pixels). The second and the third functions will be realized with two fast scintillator detectors placed downstream of the TPC&FT detector. Also, a high-pressure ionization chamber will be used for the beam current control and for evaluation of the pile-up correction in the absolute counting of the beam rate by the SC detectors (the beam rate will be around 2 MHz). The upstream beam detectors (SC detectors and pixels) will be used only for calibration purposes, and they will be in the out-of-beam position during the physics runs in order to reduce the amount of material in the beam line. The beam enters the TPC through a 400 μm Be window.

With this system, the integrated beam rate will be measured with 0.1% absolute precision.

The beam parameters are presented in Table 1.

Table 1
Parameters of the electron beam planned to use in this experiment

Beam energy	720 MeV
Beam energy resolution	< 20 keV (1σ)
Absolute beam energy precision	± 150 keV (1σ)
Beam intensity (main run)	$2 \cdot 10^6$ e/s
Beam intensity for calibration	10^4 e/s and 10^3 e/s
Beam divergency	≤ 0.5 mrad (1σ)
Beam size	≤ 0.2 mm (1σ)
Duty factor	100%

The gas pressure in the TPC will be measured with 0.01% absolute precision. The temperature of the detector body will be maintained constant at 298⁰ K with a special thermo-stabilization system, and it will be measured with 0.015% absolute precision. ***This determines the proton density with 0.025% absolute precision.*** The electron drift velocity W in the TPC will be measured directly in this experiment with precision 0.01%. The maximal drift time is ~ 90 μ s. The gas target length is determined from the measured difference between the maximal and minimal arrival times of the TPC signals in the chosen drift space, $L_{\text{tag}} = (t_{\text{R max}} - t_{\text{R min}}) \times W$. ***The expected precision in determination of L_{tag} is 0.02% for $L_{\text{tag}} = 35$ cm.*** Note that thus selected hydrogen gas target is separated from the grid and from the cathode, therefore there are no wall effects in the measurements.

Recoil energy (T_{R}), angle (θ_{R}) and arrival time (t_{R}) resolution. The anode channels will be equipped with low-noise preamplifiers with the noise at the level of 20 keV (sigma). The beam induced noise is essential only at the central pad where it is expected to be around 80 keV for the main run conditions (20 bar hydrogen, 2 MHz beam rate). The expected recoil arrival time resolution is 40 ns. The recoil angle will be determined by the difference in arrival times of the signals from the neighbour pads (possible for proton ranges exceeding 60 mm). The recoil angular resolution will be from 15 mrad to 10 mrad.

Vertex position and resolution. The z -coordinate of the vertex Z_{V} is determined by the drift time t_{R} and the drift velocity W with ± 100 μ m absolute precision. The X_{V} and Y_{V} coordinates are distributed around the central values $X_{\text{V}} = 0$ and $Y_{\text{V}} = 0$ determined by the beam position along the TPC axis, the deviations being caused by the beam size (~ 200 μ m), beam divergence (~ 0.5 mrad), and the Coulomb scattering (~ 0.5 mrad).

Angle θ_{e} of scattered electrons, absolute value and resolution. The angle θ_{e} of a scattered electron is determined by the vertex coordinate Z_{V} and the $X1/Y1$ coordinates in the Forward Tracker with the resolution ~ 1 mrad (beam divergence and Coulomb scattering).

The centre-of-gravity of the θ_{e} distribution corresponding to a selected recoil energy T_{R} is measured with 0.02% precision determined mainly by the absolute precision in measurements of the $X1/Y1$ coordinates.

4. Measurement procedure

The ep differential cross section is determined by the transfer momentum and is practically independent of the electron energy at $\varepsilon_{\text{e}} \geq 500$ MeV in the considered low Q^2 region. The transfer momentum $-t = Q^2$ can be determined either by the recoil proton energy T_{R} or by the electron scattering angle θ_{e} . The advantage of the T_{R} method is determination of the transfer momentum independently of the electron energy ε_{e} :

$$-t = 2MT_{\text{R}}. \quad (3)$$

Therefore, measuring the transfer momentum by the T_{R} method, we avoid the influence of the beam energy losses before the ep collision (as well as the initial beam energy spread) on the measured $d\sigma/dt$. This is especially important for the ep scattering because of the radiation losses of the electrons in the materials upstream of the ep collision point. On the contrary, the transfer momentum determined *via* the electron scattering angle θ_{e} depends on ε_{e} :

$$-t = \frac{4e_e^2 \sin^2 \frac{\mathcal{J}}{2}}{1 + \frac{2e_e \sin^2 \frac{\mathcal{J}}{2}}{M}}. \quad (4)$$

A possible tail in ε_e results in a tail in the measured Q^2 distribution (Fig. 5) and thus disturbs the $d\sigma/dt$ measurement. On the other hand, the θ_e scale can be fabricated with high absolute precision. This allows to perform a precise T_R scale calibration using the measured $\theta_e - T_R$ correlation plot. We call this procedure as *self-calibration of the T_R scale* as it does not require any special measurements and can be performed using the full set of the collected experimental data. This is an essential point of our experimental method. The electron scattering angle is measured with 0.02% precision which allows to calibrate *the T_R scale with 0.04% relative precision*. Furthermore, the absolute energy of the 720 MeV electron beam is known with 0.02% precision. This means that *the T_R scale can be calibrated with 0.08% absolute precision*.

Another advantage of the recoil method is relatively small radiative corrections to the measured value of $d\sigma/dt$. Figure 5 (left panel) shows the main diagrams of the radiative processes in the ep scattering. In the previous experiments, where the transfer momentum was determined by measuring the angle and the momentum of the scattered electron, the main contributions to the radiative corrections came from diagrams v2, r1, and r2. On the contrary, they cancel each other almost exactly when the transfer momentum is determined by the recoil energy T_R (under condition that there are no cuts introduced in the scattered electron distributions). Figure 5 (right panel) demonstrates the radiative tail in the θ_e distribution corresponding to a selected recoil energy around $T_R = 5$ MeV. This tail is within the acceptance of the Forward Detector. In the analysis, when calculating $d\sigma/dt$, it can be included into the total number of events corresponding to the selected ΔT_R , while the transfer momentum (used for the T_R scale calibration) is determined by the peak position ($\theta_{e \text{ max}}$) in the θ_e distribution. The remaining radiative corrections can be calculated with rather high accuracy. Moreover, they can be controlled by the absolute measurements of $d\sigma/dt$ planned in this experiment.

Elimination of the background reactions. The $T_R - \theta_e$, $T_R - \theta_R$, and $\theta_R - \theta_e$ correlations can be used to eliminate the backgrounds. As an example, Figure 6 demonstrates these correlation plots calculated for the ep elastic scattering and for the background reaction $ep \rightarrow ep\pi^0$ for 720 MeV electrons. One can see that the elastic scattering can be well separated from the background.

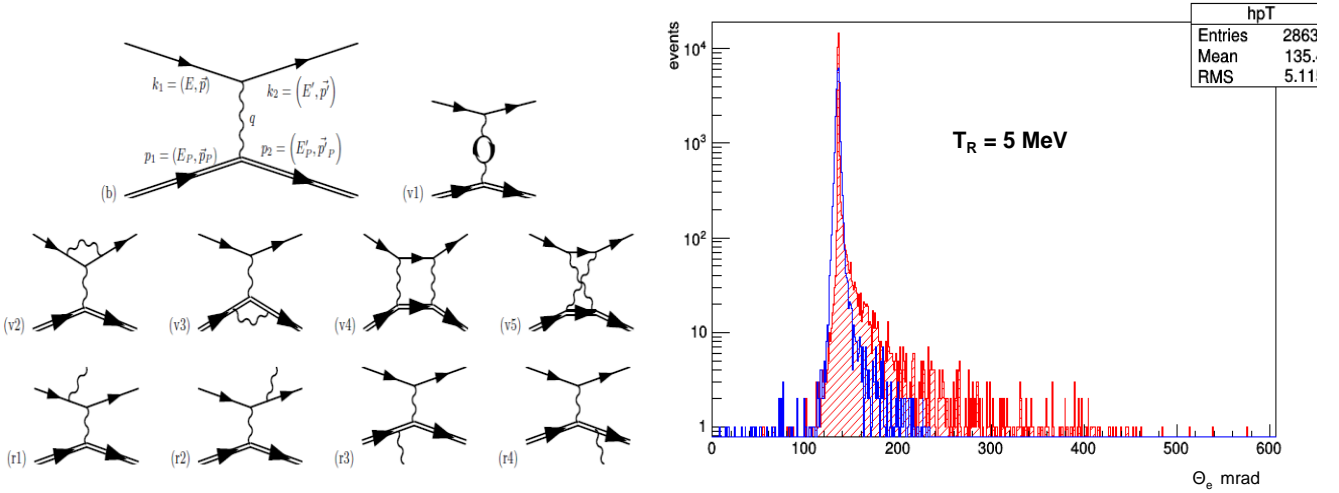


Fig. 5. Left panel: main diagrams for radiative processes in ep elastic scattering. Right panel: angular distribution of 720 MeV electrons after ep collisions calculated with the ESEPP generator taking into account all radiative corrections (red colour). This distribution corresponds to the selected recoil energy around $T_R = 5$ MeV. For comparison, the angular distribution of the electrons due to multiple Coulomb scattering is shown in blue colour

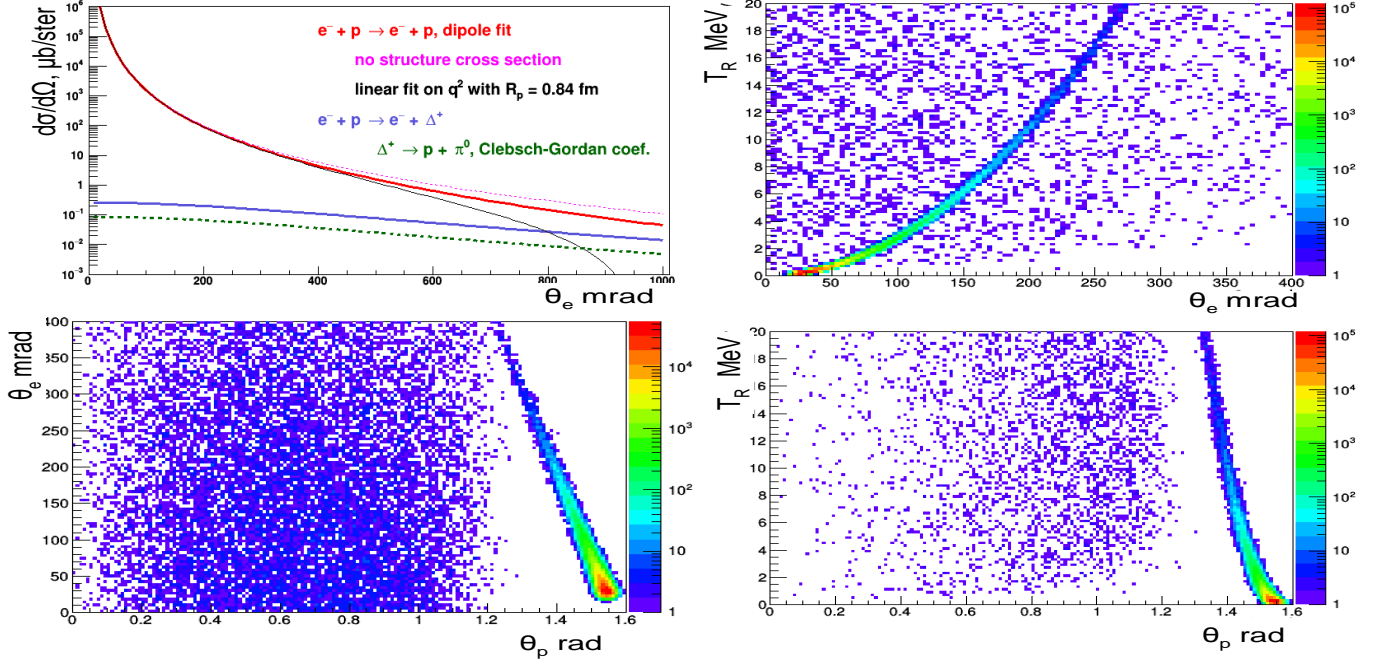


Fig. 6. The $T_R - \theta_e$ (upper right), $T_R - \theta_p$ (bottom right), and $\theta_R - \theta_e$ (bottom left) correlation plots calculated for elastic ep scattering and for the background reaction $ep \rightarrow ep\pi^0$ at $\varepsilon_e = 720$ MeV. Also shown are the differential cross sections for elastic and inelastic ep scattering (upper left). Note that θ_p in these plots corresponds to $90^\circ - \theta_R$

Trigger and acquisition. An adjustable combination of signals from the TPC anodes exceeding some threshold values will be used for triggering the readout system (*the TPC self-triggering mode*). This is the most safe and effective triggering option. The expected trigger rate will be around 50 Hz. The acquisition system will provide continuous data flow without introducing any dead time. After receiving a trigger signal, the information from all detectors which appeared in a 100 μs time interval before the arrival of the trigger is readout from the pipeline and sent to DAQ. The efficiency in detection of the ep events triggered by the TPC should be close to 100% in the measured t -range.

Selection of true ep collisions. The trigger is a recoil signal ($T_R \geq 0.3$ MeV) detected in the TPC at the time t_R . The maximum drift time in the TPC is 100 μs . Therefore, any beam electron appearing in the TPC in the time interval $t_R - 100 \mu\text{s} \leq t \leq t_R$ should be considered as a candidate for the recoil parent particle. The electron beam intensity is $2 \cdot 10^6$ electrons per second. This means that the average number of the ep candidates at this stage is 200. The selection of the true ep scattering event is needed for finding the correct Z_V coordinate of the ep collision vertex. This selection will be done in the off-line analysis applying the following criteria. First, the requirement of a track detected in the Forward Tracker (outside the 2 cm central dead area) in the 100 μs time window before arrival of the trigger signal will reduce the number of the ep candidates by a factor of 40. The remaining candidates with arrival times t_i correspond to different coordinates of the ep vertex: $Z_i = W \times (t_R - t_i)$ where W is the drift velocity. Tracing back the electron trajectory determined by the FT1 and FT2 planes, one can determine the Z_{back} coordinate and compare it with Z_i . According to MC simulations, after this selection less than one false candidate in average remains per one true ep event. Finally, the $\theta_e - T_R$ correlation provides a powerful background rejection. Together with the previous selection steps, this allows to select the true ep events on a high confidence level with $\sim 100\%$ detection efficiency.

Statistics and beam time. The statistical error in the measured proton radius was estimated by simulation of $7 \cdot 10^7$ ep scattering events in the Q^2 -range from 0.001 GeV^2 to 0.04 GeV^2 (Integrated luminosity $2.81 \cdot 10^8 \text{ mb}^{-1}$). Such a number of events could be collected during 45 days of continuous running in the $2 \cdot 10^6$ e/s beam with the TPC operating at 20 bar with 35 cm target length ($3.6 \cdot 10^{22}$ protons/ cm^2). For this analysis, $d\sigma/dt$ was generated assuming $G_M(Q^2) = \mu_p G_E(Q^2)$, where μ_p is the proton magnetic moment. Both form factors were represented by a modified Dipole Form Factor corresponding to a fixed value of $R_{pE} = R_{pM} = \langle R_p^2 \rangle^{1/2} = 0.8775$ fm:

$$G(Q^2)/G(0) = (1 + Q^2/0.6068)^{-2}. \quad (5)$$

The generated $d\sigma/dt$ was fitted using $d\sigma/dt_{\text{fit}}$ with the form factors represented by a power series expansion:

$$G(Q^2)/G(0) = A (1 + \sum_{n=1}^{n_{\text{max}}} C_n \cdot Q^{2n}), \quad (6)$$

where $C_n = (-1)^n \langle R_p^{2n} \rangle / (2n+1)! \cdot (0.1973)^{2n}$. Here Q^{2n} and $\langle R_p^{2n} \rangle$ are expressed in GeV^{2n} and in fm^{2n} , respectively. The parameters A , $\langle R_p^2 \rangle$, and $\langle R_p^4 \rangle$ were the fitting parameters. The parameter $\langle R_p^6 \rangle$ was fixed to various values to study the sensitivity of the extracted R_p to this parameter. Also, it could be used as an additional free parameter in the fits. Figure 7 (left panel) presents the results of the fit performed without the Q^6 term in expression (6), that is for $\langle R_p^6 \rangle = 0$. A similar analysis was done with 100 times higher statistics to estimate a possible systematic bias which could be related with neglecting the Q^6 and higher terms in the power series expansion of the fit function. The results are presented in Fig. 7 (right panel).

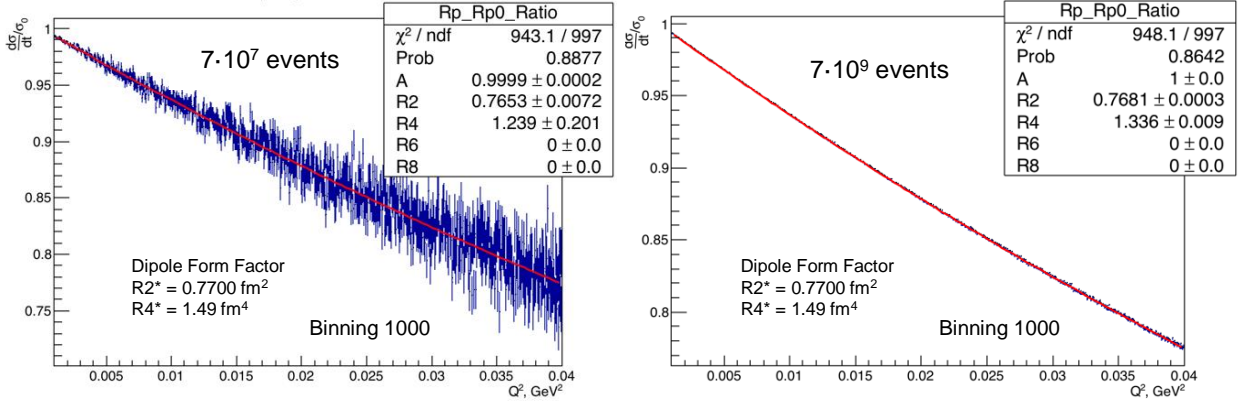


Fig. 7. Fitting of the ratio $R = d\sigma/dt (R_p = 0.8775 \text{ fm}) / d\sigma/dt (R_p = 0)$ in the Q^2 range $0.001 \text{ GeV}^2 \leq Q^2 \leq 0.04 \text{ GeV}^2$. The cross section $d\sigma/dt$ was generated with the electric and magnetic form factors represented by Eq. (5). The fit function $G(Q^2)_{\text{fit}} / G(0)$ was taken as a power series expansion (6) with $n_{\text{max}} = 2$, ($\langle R_p^6 \rangle = 0$). *Left panel:* fit to $d\sigma/dt$ generated with the statistics foreseen for this experiment, $7 \cdot 10^7$ events. *Right panel:* a similar fit with 100 times higher statistics, $7 \cdot 10^9$ events. Shown in this figure R2, R4, R6, R8 stand for $\langle R_p^2 \rangle$, $\langle R_p^4 \rangle$, $\langle R_p^6 \rangle$, $\langle R_p^8 \rangle$, respectively. In terms of the power series expansion, the Dipole Form Factor used in this analysis corresponds to $\langle R_p^2 \rangle = 0.7700 \text{ fm}^2$, $\langle R_p^4 \rangle = 1.49 \text{ fm}^4$, $\langle R_p^6 \rangle = 5.3 \text{ fm}^6$

As it follows from Fig. 7 (left panel), the statistical error in determination of $R2 = \langle R_p^2 \rangle$ is $0.0072 / 0.7700 = 0.93\%$, which corresponds to a 0.47% error in determination of R_p . The systematic bias shown in Fig. 7 (right panel) is $\Delta R2 = 0.7681 \text{ fm}^2 - 0.7700 \text{ fm}^2 = -0.0019 \text{ fm}^2$. This corresponds to a 0.12% systematic bias in measurement of R_p ($\pm 0.001 \text{ fm}$).

This consideration shows that, if the proton form factor could be represented by the Dipole Form Factor, the Q^6 term can be neglected in the fit function without noticeable influence on the measured proton radius. However, previous analyses of the existing ep scattering data showed that contributions of the higher terms of the power series expansion of the proton form factor may be considerably larger than those in the Dipole Form Factor. In particular, J. Bernauer [5,10] has obtained the following results from the analysis of the A1 experiment data using a tenth order power series expansion of the proton form factor:

$$\langle R_p^2 \rangle = 0.774(8) \text{ fm}^2, \quad \langle R_p^4 \rangle = 2.59(19)(04) \text{ fm}^4, \quad \langle R_p^6 \rangle = 30(7.6)(12.6) \text{ fm}^6, \quad \langle R_p^8 \rangle = 372 \text{ fm}^8.$$

Based on these results, we have analysed the sensitivity of the extracted value of the proton radius R_p to variations of $\langle R_p^4 \rangle$ from 2.4 fm^4 to 2.8 fm^4 and $\langle R_p^6 \rangle$ from 11 fm^6 to 41 fm^6 in the generated $d\sigma/dt$ with the form factors represented by the power series expansion (6) with fixed values of $\langle R_p^2 \rangle = 0.7700 \text{ fm}^2$ and $\langle R_p^8 \rangle = 372 \text{ fm}^8$. Similarly, the fit function $d\sigma/dt_{\text{fit}}$ contained the form factors parametrized by the power series expansion with A , $\langle R_p^2 \rangle$, and $\langle R_p^4 \rangle$ used as free parameters, and $\langle R_p^6 \rangle$ as a variable fixed parameter. It was shown that, with the $\langle R_p^6 \rangle$ value fixed around 26 fm^6 , the above mentioned variations of $\langle R_p^4 \rangle$ and $\langle R_p^6 \rangle$ in the simulated $d\sigma/dt$ resulted in $\pm 0.0025 \text{ fm}$ systematic bias in the value of the proton radius R_p extracted with the statistical error of $\pm 0.0041 \text{ fm}$.

Fits with four free parameters (A , $\langle R_p^2 \rangle$, $\langle R_p^4 \rangle$, and $\langle R_p^6 \rangle$) allow to extract the proton radius with very low systematic bias ($\leq 0.001 \text{ fm}$) but with larger statistical errors ($\pm 0.0085 \text{ fm}$).

5. Summary of systematic errors

Table 2 summarizes the expected systematic errors in various components critical for measurements of the relative and absolute differential ep elastic scattering cross sections in the Q^2 -range from 0.001 GeV² to 0.04 GeV² with 0.1% and 0.2% precision, respectively.

Table 2
Summary of systematic errors expected in the proposed experiment

		Syst. Error %	comment
1	Drift velocity, $W1$	0.01	
2	High Voltage, HV	0.01	
3	Temperature, K	0.015	
4	Pressure, P	0.01	
5	H ₂ density, ρ_p	0.025	Sum of errors 3 and 4
6	Target length, L_{tag}	0.02	
7	Number of protons in target, N_p	0.045	Sum of errors 5 and 6
8	Number of beam electrons, N_e	0.05	Beam detector counts corrected for pileups
9	Detection efficiency of ep events	0.05	
10	Electron beam energy, ϵ_e	0.02	
11	Electron scattering angle, θ_e	0.02	
12	t -scale calibration, T_R relative	0.04	Follows from error 11
13	t -scale calibration, T_R absolute	0.08	Follows from the sum of errors 11 and 10
	$d\sigma/dt$, relative	0.1	0.08% from error 12
	$d\sigma/dt$, absolute	0.2	0.16% from error 13 plus errors 7, 8, 9

6. Conclusion

This project is designed for measurements of differential cross sections for the electron-proton elastic scattering in the transfer momentum region $0.001 \text{ GeV}^2 \leq Q^2 \leq 0.04 \text{ GeV}^2$ with 0.1% relative and 0.2% absolute precision. The experimental method is based on measurements of the energy of the recoiled proton and the angle of the scattered electron. One of the advantages of this method is relatively low radiative corrections to the measured cross sections. These measurements should allow to extract the proton charge radius with a sub-percent precision that could be decisive for solving the ‘‘proton radius puzzle’’. The experiment will be performed in the 720 MeV electron beam of the Mainz electron accelerator MAMI.

References

1. R. Pohl *et al.*, Nature **466**, 213 (2010).
2. A. Antognini *et al.*, Science **339**, 417 (2013).
3. J.C. Bernauer *et al.*, Phys. Rev. Lett. **105**, 242001 (2010).
4. X. Zhan *et al.*, Phys. Lett. B **705**, 59 (2014).
5. I. Sick and D. Trautmann, Phys. Rev. C **95**, 012501 (2017).
6. H. Gao, C. Peng, EPJ Web Conf. **113**, 03007 (2016).
7. J.P. Burq *et al.*, Nucl. Phys. B **217**, 285 (1983).
8. A.V. Dobrovolsky *et al.*, Nucl. Phys. A **766**, 1 (2006).
9. V.A. Andreev *et al.*, Phys. Rev. Lett. **110**, 022504 (2013).
10. J.C. Bernauer, Ph. D. Theses, University of Mainz, 2010.